UC Davis
UC Davis Previously Published Works

Title

State-to-state vacuum ultraviolet photodissociation study of CO 2 on the formation of state-correlated CO(X 1 Σ + ; v) with O(1 D) and O(1 S) photoproducts at 11.95—12.22 eV

Permalink

https://escholarship.org/uc/item/4zb4z3j7

Journal

Physical Chemistry Chemical Physics, 17(17)

ISSN

1463-9076

Authors

Lu, Zhou
Chang, Yih Chung
Benitez, Yanice
et al.

Publication Date

2015-05-07

DOI

10.1039/c5cp01321f

Peer reviewed

eScholarship.org Powered by the California Digital Library
University of California

PCCP

PAPER

Cite this: *Phys. Chem. Chem. Phys.*, 2015, **17**, 11752

State-to-state vacuum ultraviolet photodissociation study of CO_2 on the formation of state-correlated $CO(X^1\Sigma^+; v)$ with $O(^1D)$ and $O(^1S)$ photoproducts at 11.95–12.22 eV†

Zhou Lu,[a] Yih Chung Chang,[a] Yanice Benitez,[a] Zhihong Luo,[a] Adel Ben Houria,[b] Tarek Ayari,[b] Muneerah Mogren Al Mogren,[c] M. Hochlaf,*[d] W. M. Jackson*[a] and C. Y. Ng*[a]

The state-to-state photodissociation of CO_2 is investigated in the VUV range of 11.94–12.20 eV by using two independently tunable vacuum ultraviolet (VUV) lasers and the time-sliced velocity-map-imaging-photoion (VMI-PI) method. The spin-allowed $CO(X^1\Sigma^+; v = 0–18) + O(^1D)$ and $CO(X^1\Sigma^+; v = 0–9) + O(^1S)$ photoproduct channels are directly observed from the measurement of time-sliced VMI-PI images of $O(^1D)$ and $O(^1S)$. The total kinetic energy release (TKER) spectra obtained based on these VMI-PI images shows that the observed energetic thresholds for both the $O(^1D)$ and $O(^1S)$ channels are consistent with the thermochemical thresholds. Furthermore, the nascent vibrational distributions of $CO(X^1\Sigma^+; v)$ photoproducts formed in correlation with $O(^1D)$ differ significantly from that produced in correlation with $O(^1S)$, indicating that the dissociation pathways for the $O(^1D)$ and $O(^1S)$ channels are distinctly different. For the $O(^1S)$ channel, $CO(X^1\Sigma^+; v)$ photoproducts are formed mostly in low vibrational states (v = 0–2), whereas for the $O(^1D)$ channel, $CO(X^1\Sigma^+; v)$ photoproducts are found to have significant populations in high vibrationally excited states (v = 10–16). The anisotropy β parameters for the $O(^1D) + CO(X^1\Sigma^+; v = 0–18)$ and $O(^1S) + CO(X^1\Sigma^+; v = 0–9)$ channels have also been determined from the VMI-PI measurements, indicating that CO_2 dissociation to form the $O(^1D)$ and $O(^1S)$ channels is faster than the rotational periods of the VUV excited CO_2 molecules. We have also calculated the excited singlet potential energy surfaces (PESs) of CO_2, which are directly accessible by VUV excitation, at the *ab initio* quantum multi-reference configuration interaction level of theory. These calculated PESs suggest that the formation of $CO(X^1\Sigma^+) + O(^1S)$ photoproducts occurs nearly exclusively on the $4^1A'$ PES, which is generally repulsive with minor potential energy ripples along the OC–O stretching coordinate. The formation of $CO(X^1\Sigma^+) + O(^1D)$ photofragments can proceed by non-adiabatic transitions from the $4^1A'$ PES to the lower $3^1A'$ PES of CO_2 *via* the seam of conical intersections at a near linear OCO configuration, followed by the direct dissociation on the $3^1A'$ PES. The theoretical PES calculations are consistent with the experimental observation of prompt CO_2 dissociation and high rotational and vibrational excitations for $CO(X^1\Sigma^+)$ photoproducts.

Received 6th March 2015,
Accepted 30th March 2015

DOI: 10.1039/c5cp01321f

www.rsc.org/pccp

I. Introduction

The atmospheric concentration of carbon dioxide (CO_2) is increasing annually due to anthropogenic activities such as the combustion of fossil fuels and deforestation. This elevation of CO_2 concentration is considered a strong driver to global warming. The motivation for the present VUV photodissociation study of CO_2 stems in part from a desire to unravel and understand key primary photochemical processes of CO_2 induced by solar VUV excitation in the Earth's thermosphere.[1] The photodissociation of CO_2 can be considered as a sink of CO_2. Primary photodissociation channels identified in the present study are

[a] *Department of Chemistry, University of California, Davis, CA 95616, USA. E-mail: wmjackson@ucdavis.edu, cyng@ucdavis.edu*
[b] *Laboratoire de Spectroscopie Atomique, Moléculaire et Applications – LSAMA, Université de Tunis El Manar, Tunis, Tunisia*
[c] *Chemistry Department, Faculty of Science, King Saud University, PO Box 2455, Riyadh 11451, Kingdom of Saudi Arabia*
[d] *Université Paris-Est, Laboratoire Modélisation et Simulation Multi Echelle, MSME UMR 8208 CNRS, 5 bd Descartes, 77454 Marne-la-Vallée, France. E-mail: hochlaf@univ-mlv.fr*

† Electronic supplementary information (ESI) available. See DOI: 10.1039/c5cp01321f

 This journal is © the Owner Societies 2015

applicable for modeling the chemical evolution in CO_2-heavy atmospheres of solar planets, such as Venus,[2] Mars[3] and comets.[4]

Carbon dioxide has negligible photoabsorption at photon energies below ≈6.2 eV; and the CO_2 absorption bands in the VUV photon energy [$h\nu$(VUV)] range of 6.2–11.0 eV are also very weak. The major photodissociation processes of CO_2 are expected to occur at $h\nu$(VUV) > 11.00 eV, where CO_2 has significantly higher absorption cross sections.[5] The energetically accessible CO + O photoproduct channels from CO_2 photodissociation at $h\nu$(VUV) < 12.0 eV are listed below in processes (1)–(4) along with their corresponding energetic thresholds:

$$CO_2 + h\nu(\mathrm{VUV}) \rightarrow CO(X^1\Sigma^+) + O(^3P) \quad h\nu(\mathrm{VUV}) \geq 5.45\ \mathrm{eV} \tag{1}$$

$$CO_2 + h\nu(\mathrm{VUV}) \rightarrow CO(X^1\Sigma^+) + O(^1D) \quad h\nu(\mathrm{VUV}) \geq 7.42\ \mathrm{eV} \tag{2}$$

$$CO_2 + h\nu(\mathrm{VUV}) \rightarrow CO(X^1\Sigma^+) + O(^1S) \quad h\nu(\mathrm{VUV}) \geq 9.64\ \mathrm{eV} \tag{3}$$

$$CO_2 + h\nu(\mathrm{VUV}) \rightarrow CO(a^3\Pi) + O(^3P) \quad h\nu(\mathrm{VUV}) \geq 11.46\ \mathrm{eV} \tag{4}$$

Currently, the photodissociation channels of CO_2 adopted for the simulation of atmospheric evolutions of CO_2-heavy solar planets are based on previous VUV photodissociation studies of Lawrence[6,7] and Slanger *et al.*[8] Their studies indicate that the quantum yield for the formation of the spin-allowed $CO(X^1\Sigma^+)$ + $O(^1S)$ [process (3)] and $CO(a^3\Pi)$ + $O(^3P)$ [process (4)] channels is close to unity in the $h\nu$(VUV) excitation range of 11.3–13.8 eV (90–110 nm).[9] The direct experimental observation of the $CO(X^1\Sigma^+)$ + $O(^1D)$ channel [process (2)] has not been reported until the recent detection of $O(^1D)$ from CO_2 photodissociation at $h\nu$(VUV) = 13.45 eV (92.21 nm) using the VUV laser velocity-map-imaging-photoion (VMI-PI) method. In the latter experiment, Pan *et al.* used a single tunable VUV laser beam to perform both photodissociation of CO_2 molecules and photoionization detection of nascent $O(^1D)$ atomic photofragments.[10] Using the same VUV laser VMI-PI apparatus, Song *et al.* have later examined CO_2 photodissociation at $h\nu$(VUV) = 13.540–13.678 eV (90.6–91.6 nm) and have successfully detected additional energetically accessible CO + O photoproduct channels, including $CO(a'^3\Sigma^+)$ + $O(^3P)$, $CO(d^3\Delta)$ + $O(^3P)$, $CO(e^3\Sigma^-)$ + $O(^3P)$, and $CO(a^3\Pi)$ + $O(^1D)$.[11] However, the lowest photodissociation channel [process (1)] was not detected in the latter experiment.

Recently, we have implemented a second independently tunable VUV laser to the VUV laser VMI-PI apparatus, and have observed significant enhancement in experimental sensitivity for performing state-to-state photodissociation measurements of simple atmospheric molecules, such as CO_2, by using the VUV-pump and VUV-probe approach. Employing this newly established VUV–VUV laser VMI-PI apparatus, we have introduced the two-color VUV-visible (VUV-VIS) or VUV-ultraviolet (VUV-UV) laser (1 + 1′) and the single-photon VUV-excited-autoionizing-Rydberg (VUV-EAR) detection schemes for the measurement of fine-structure distributions of nascent $C(^3P_{0,1,2})$ and $O(^3P_{0,1,2})$ atomic photofragments produced by CO_2 photodissociation. The latter experiment has yielded spin–orbit resolved branching ratios for the spin-forbidden $CO(X^1\Sigma^+)$ + $O(^3P_{0,1,2})$ and spin-allowed $CO(a^3\Pi)$ + $O(^3P_{0,1,2})$ channels from CO_2 photodissociation at $h\nu$(VUV) = 12.145 eV.[12] Furthermore, in the most recent VUV–VUV laser VMI-PI study of CO_2, Lu *et al.* has provided convincing experimental evidence for the formation of correlated $C(^3P_{0,1,2})$ + $O_2(X^3\Sigma_g^-)$ photoproducts at $h\nu$(VUV) = 11.566–12.215 eV (101.5–107.2 nm).[13] This series of VUV and VUV–VUV laser VMI-PI experiments suggests that many newly identified photoproduct channels should be included in the CO_2 photodissociation network used for modeling the chemical evolution of planetary atmospheres.

Despite of the theoretical advances in the development of accurate *ab initio* quantum computation procedures and chemical dynamics calculations for small molecules, it remains a challenging task to predict the branching ratios of photodissociation channels of simple molecules from first-principle theoretical calculations. In addition to the practical utilization of atmospheric simulations, an important goal of the present photodissociation study of CO_2 is to provide reliable state-to-state data for benchmarking state-of-the-art theoretical photodissociation dynamics calculations.

Parallel to the experimental studies, theoretical efforts have also been made to calculate reliable CO_2 potential energy surfaces (PESs) involved, aiming to provide insight into the pathways of CO_2 photodissociation. Hwang and Mebel have performed *ab initio* calculations of the lowest singlet and triplet PESs of CO_2 at the G2(MP2) level of theory.[14] Their calculation predicts the direct formation of molecular oxygen O_2 on the singlet ground state PES *via* a cyclic [c-$CO_2(^1A_1)$] and a linear [$COO(^1\Sigma^+)$] intermediates. More recently, Schmidt *et al.* have constructed the CO_2 PESs in the VUV energy range of 5.90–8.27 eV at the internally contracted multi-reference configuration interaction (MRCI) level of theory in order to elucidate the dissociation pathways, leading to the formation of the spin-allowed $CO(X^1\Sigma^+)$ + $O(^1D)$ and the spin-forbidden $CO(X^1\Sigma^+)$ + $O(^3P)$ channels.[15] Partly due to the valence-Rydberg nature of the excited states, the calculation of the PESs can be difficult. Very recently, Grebenshchikov reported on the 3-dimensional PESs of six singlet valence electronic states between 7.75 and 10.33 eV. These calculations show that non-adiabatic dissociation mechanisms may involve multiple conical intersections or seams of conical intersections.[16,17] At sufficiently higher photodissociation energies, where many PESs and photodissociation channels are involved, the photodissociation dynamics for even diatomic or triatomic molecules can be exceedingly complex and must be considered as a complex system.

The present article is concerned with a detailed study of the CO_2 photodissociation dynamics leading to the formation of the $CO(X^1\Sigma^+)$ + $O(^1D)$ and $CO(X^1\Sigma^+)$ + $O(^1S)$ channels at $h\nu$(VUV) = 11.95–12.22 eV. By recording the $O(^1D)$ and $O(^1S)$ VMI-PI images observed at selected VUV excited CO_2 dissociative states, we have determined the vibrational state distributions of the counter $CO(X^1\Sigma^+; v)$ photofragments. The VMI-PI images thus obtained also allow the determination of the anisotropy β parameters for the $O(^1D)$ and $O(^1S)$ channels, which in turn

provide the estimates of the CO_2 photodissociation lifetimes with respect to the rotational periods of the VUV excited CO_2* molecules. In this work, we have also performed high-level MRCI *ab initio* calculations on the excited singlet potential energy surfaces (PESs) of CO_2, which are directly accessible by VUV excitation. The features of the calculated PESs are consistent with the state-to-state experimental results observed in the present VUV–VUV laser VMI-PI study and have provided valuable insight into the dynamics of CO_2 photodissociation.

II. Experimental considerations

The experimental arrangement and procedures of using the VUV–VUV laser VMI-PI apparatus have been described in detail previously.[10–13,18–20] Briefly, the apparatus consists of two independently tunable VUV lasers, a molecular beam production system, and a VMI-PI detector. In general, an Even-Lavie valve (EL-5-2004, nozzle diameter = 0.2 mm) operating at 30 Hz was used to generate a supersonic molecular beam consisting of ~10% CO_2 seeded in He. The skimmed molecular beam was irradiated by two tunable, unfocused VUV lasers, which are designated as VUV_1 and VUV_2 laser beams, in the photodissociation/photoionization (PD/PI) center of the VMI-PI apparatus. The VUV_1 laser beam is used to excite CO_2 molecules to a specific excited CO_2* dissociative state, *i.e.*, $CO_2 + h\nu(VUV_1) \rightarrow CO_2^* \rightarrow CO + O$. The VUV_2 laser beam is tuned to selectively photoionize $O(^1D)$ or $O(^1S)$ atomic photofragments *via* the VUV-EAR scheme. Both VUV_1 and VUV_2 laser systems have a similar design and are generated by two-photon resonance-enhanced four-wave sum and difference-frequency mixings, $2\omega_1 \pm \omega_2$, using a pulsed Kr or Xe jet as the nonlinear medium.[19] The VUV laser outputs have an optical bandwidth of 0.4 cm^{-1} (full-width at half-maximum, FWHM). In this experiment, the $2\omega_1$ frequency corresponds to the two-photon resonant frequency of Xe at 249.629 nm or Kr at 202.316 nm and 212.556 nm. The employment of the VUV_2 photoionization laser pulse was delayed by 10–20 ns with respect to the VUV_1 photodissociation laser pulse. The photoions resulting from the intersections of the CO_2 molecular beam and the VUV_1 and VUV_2 laser beams were accelerated by a set of ion imaging lenses down a 75 cm flight tube onto a position-sensitive dual microchannel plate detector. Individual $O(^1S)$ and $O(^1D)$ VMI-PI images were accumulated for 30 000 and 90 000 laser shots, respectively.

III. Computational considerations

All *ab initio* quantum calculations were carried out using the MOLPRO program suite in the C_s point group.[21] For these calculations, the generally contracted aug-cc-pV5Z basis of Dunning and co-workers were used for the description of C and O atoms.[22–25] It results in 381 contracted Gaussian type functions.[22] In the present study, we have mapped the PESs of the lowest singlet states of CO_2, including the four lowest A′ and three lowest A″ states. These PESs have been generated using the complete active space self-consistent field (CASSCF)[26–28] method, followed by the internally contracted MRCI approach.[29,30] In CASSCF calculations, the three lowest a′ orbitals were optimized but kept doubly occupied, in order to reduce the size of these calculations. This results in more than 35×10^3 Configurations State Functions (CSFs) to be considered in each symmetry of the C_s point group. All valence electrons were correlated. In these calculations, the electronic states having the same spin multiplicity were averaged together using the averaging procedure implemented in the MOLPRO program. For MRCI calculations, all configurations having a weight ≥ 0.05 in the CI expansion of the CASSCF wavefunctions were taken into account as a reference. This leads to more than 1.6×10^8 (2×10^7) uncontracted (contracted) CSFs to be considered per C_s symmetry. The energies were then fitted using bi dimensional spline functions. The root mean square of the fit achieved was smaller than 1 meV.

IV. Results and discussion

A. Comparison of the $O(^1S)$ and $O(^1D)$ photofragment excitation and CO_2 absorption spectra

Fig. 1(a)–(c) depict the respective high-resolution photoabsorption spectrum of CO_2 recorded by Archer *et al.*,[31] the $O(^1S)$ photofragment excitation (PHOFEX) spectrum, and the $O(^1D)$ PHOFEX spectrum in the photon energy range of 11.945–12.215 eV. The $O(^1S)$ and $O(^1D)$ photofragments were probed by tuning the VUV_2 laser radiation to the respective autoionization transitions of $O^*[2s^22p^3(^2P^0)3s(^1P^0_1)] \leftarrow O(^1S)$ and $O^*[2s^22p^3(^2D^0_{3/2})3d(^1D^0_2)] \leftarrow O(^1D)$. To our knowledge, the detection of the $O(^1D) + CO(X^1\Sigma^+)$

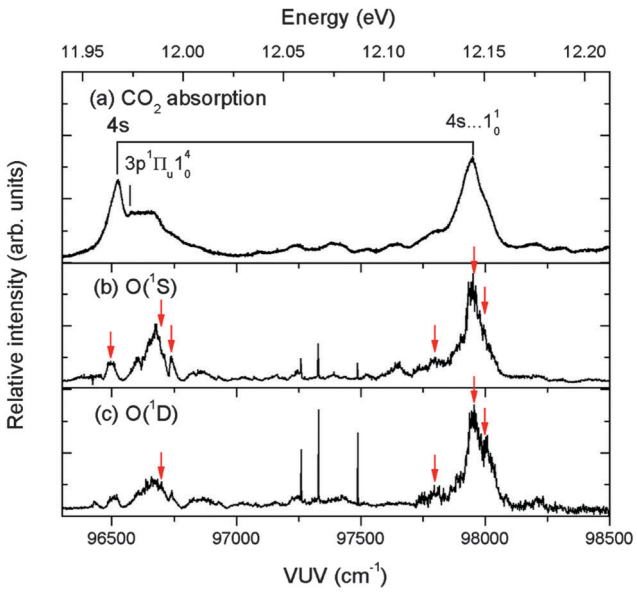

Fig. 1 Comparison of the high resolution absorption spectrum of CO_2 recorded by Archer *et al.* shown in (a) with the $O(^1S)$ PHOFEX spectrum in (b) and the $O(^1D)$ PHOFEX spectra in (c). The VUV_1 photodissociation laser energy was scanned between 96 300 and 98 500 cm^{-1}. The VUV_2 photoionization laser energy was selectively tuned to probe $O(^1S)$ and $O(^1D)$ photoproducts *via* the respective autoionization transitions of $O^*[2s^22p^3(^2P^0)3s(^1P^0_1)] \leftarrow O(^1S)$ and $O^*[2s^22p^3(^2D^0_{3/2})3d\ (^1D^0_2)] \leftarrow O(^1D)$. The VUV_1 photodissociation laser energies used for recording the $O(^1S)$ and $O(^1D)$ VMI-PI images are marked by red arrows in (b) and (c).

 This journal is © the Owner Societies 2015

channel [process (2)] from CO_2 photodissociation in the $h\nu$(VUV) range of 11.495–12.215 eV (101.5–103.8 nm) has not been reported previously. The PHOFEX spectra of Fig. 1(b) and (c) have been normalized by the VUV_1 laser intensities, which were measured by recording the C_2H_2 photoionization efficiency spectrum and comparing it to that reported previously by Dibeler and Walker.[32] Thus, the $O(^1S)$ and $O(^1D)$ PHOFEX spectra shown in Fig. 1(b) and (c) represent the relative photodissociation cross sections for the formation of $O(^1S)$ and $O(^1D)$, respectively, from different VUV_1 excited CO_2* dissociative states.

The CO_2 absorption bands covering the VUV region of interest here have been assigned previously by Cossart-Magos *et al.* to the vibrational progression of the symmetric stretching mode of the 4s and $3p^1\Pi_u$ Rydberg states of CO_2.[33] Since one quantum of the CO_2 symmetric stretching frequency is in near energy resonance with two quanta of the CO_2 bending frequency, Fermi resonance interactions occur between these vibrational modes of CO_2, resulting in the excitation of the combination of the symmetric stretching and bending modes. The photoabsorption spectrum of Fig. 1(a) mainly consists of two CO_2 absorption bands. The higher energy band (peaked at 97955.7 cm^{-1}) has been assigned as the excited CO_2* [$4s(1_0{}^1)$] Rydberg state. The lower energy band may consist of three states. As marked in Fig. 1(a), the absorption peak and the center of this band were assigned as the 4s and $3p^1\Pi_u(1_0{}^4)$ Rydberg states, respectively. The high energy shoulder at 96667.3 cm^{-1} of this absorption peak was noted by Cossart-Magos *et al.* as a possible excited CO_2* predissociative state; but the nature of this shoulder peak has not been assigned.[33]

The PHOFEX spectra of $O(^1S)$ and $O(^1D)$ shown in Fig. 1(b) and (c) are in excellent agreement with the CO_2 photoabsorption spectrum of Fig. 1(a), except that the 4s and $3p^1\Pi_u(1_0{}^4)$ Rydberg peaks of CO_2 at 11.960–12.010 eV that are observed in the absorption spectrum is strongly distorted in the $O(^1S)$ and $O(^1D)$ PHOFEX spectra due to a strong dip in the VUV_1 tuning curve centered at the $3p^1\Pi_u(1_0{}^4)$ Rydberg peak position. As a result of the lack of VUV_1 output, the PHOFEX spectra for $O(^1S)$ and $O(^1D)$ at this position appeared as a pronounced artificial dip. Furthermore, we find that the intensity of the 4s Rydberg peak identified in the $O(^1S)$ and $O(^1D)$ PHOFEX spectra is also significantly suppressed.

The PHOFEX spectra of Fig. 1(b) and (c) also reveal three intense, sharp O^+ atomic ion resonances at 97261.4, 97330.1, and 97488.5 cm^{-1}, which have been identified previously to arising from two-color VUV-VIS (1 + 1′) photoionization of $O(^3P_{0,1,2})$ *via* the intermediate O* atom Rydberg states $O^*[2s^22p^3(^4S^0)3d(^3D^0{}_{1,2,3})]$. The observation of these intense resonances reveals the highly sensitive nature of the VUV-VIS (1 + 1′) photoionization method for the detection of $O(^3P_{0,1,2})$ atomic photofragments.

B. The formation of the $O(^1S)$ + $CO(X^1\Sigma^+; v)$ photoproduct channel

The time-sliced VMI-PI images for $O(^1S)$ measured in the photodissociation of CO_2 at $h\nu(VUV_1)$ = 12.125, 12.145, and 12.150 eV are presented in Fig. 2(a)–(c), respectively. These VUV_1 photon energy settings [marked by red downward pointing arrows in Fig. 1(b)] are chosen to examine the dissociation dynamics of the excited CO_2*[$4s(1_0{}^1)$] Rydberg state. The observed $O(^1S)$ VMI-PI images reveal discernible anisotropic ring structures, suggesting that CO_2 photodissociation to form $O(^1S)$ + $CO(X^1\Sigma^+)$ photoproducts takes place on a time scale shorter than the rotational period of the VUV_1 excited CO_2* [$4s(1_0{}^1)$] state. Two detection schemes (I) and (II), corresponding to the autoionization transitions, of $O^*[2s^22p^3(^2P^0)3s(^1P^0{}_1)] \leftarrow O(^1S)$ and $O^*[2s^22p^3(^2P^0)4d(^1P^0{}_1)] \leftarrow O(^1S)$, were used to measure the time-sliced VMI-PI images for $O(^1S)$. The $O(^1S)$ VMI-PI images thus obtained using these two schemes are found to be in excellent agreement, ensuring the reliability of the $CO(X^1\Sigma^+)$ vibrational state distributions deduced from the images. The detection scheme (I) relies on the photoionization of $O(^1S)$ photoproducts using the VUV difference-frequency $(2\omega_1 - \omega_2)$ = 82125.5 cm^{-1} (10.182 eV), whereas the detection scheme (II) requires the photoexcitation of $O(^1S)$ photofragments using the VUV sum-frequency $(2\omega_1 + \omega_2)$ = 109596.7 cm^{-1} (13.588 eV). The relative O^+ ion intensities observed by using detection schemes I and II are found to be about 10 : 1.

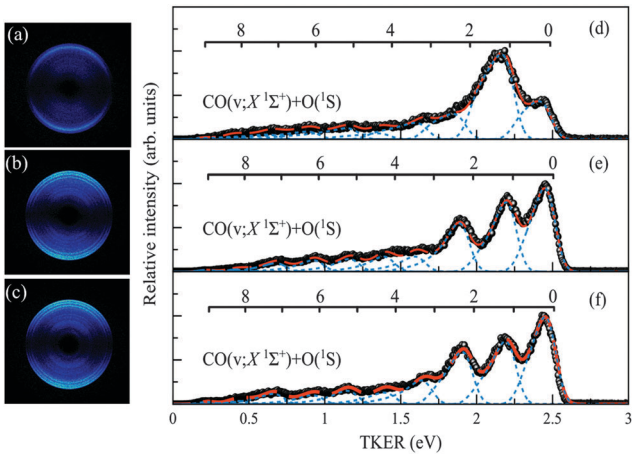

Fig. 2 Time-sliced VMI-PI images for $O(^1S)$ photofragments recorded at CO_2 photodissociation energies of (a) 97797.7 cm^{-1} (12.125 eV), (b) 97955.1 cm^{-1} (12.145 eV), and (c) 97998.1 cm^{-1} (12.150 eV) and their corresponding TKER spectra (black open-circle curves) shown in (d–f). Black drop lines on the TKER spectra designate the vibrational levels of the $CO(X^1\Sigma^+; v = 0–9)$ product. The vibrational state assignments are based on the simulated vibrational distributions (red curves), which represent the sum of individual simulated vibrational peaks (blue dashed lines).

Fig. 2(d)–(f) show the total kinetic energy release (TKER) spectra for the formation of the $CO(X^1\Sigma^+)$ + $O(^1S)$ channel transformed from the corresponding $O(^1S)$ VMI-PI images depicted in Fig. 2(a)–(c). These TKER spectra reveal a series of partially resolved vibrational peaks with the energy spacing of about 0.27 eV. Since this spacing is equal to the vibrational frequency of $CO(X^1\Sigma^+)$, we have assigned the vibrational peaks to the formation of $CO(X^1\Sigma^+; v = 0–9)$ vibrational states. Furthermore, the onsets of these TKER spectra are in excellent agreement with the known thermochemical threshold of process (3), indicating that the $CO(X^1\Sigma^+; v = 0–9)$ photofragments are produced in correlation with the $O(^1S)$ atomic photoproducts. By employing similar procedures used by Chen *et al.*,[34] we have simulated the rotational distributions of individual $CO(X^1\Sigma^+; v)$ vibrational bands

resolved in the TKER spectra of Fig. 2(d)–(f). The simulation uses a Gaussian instrumental line profile with a FWHM = 0.07 eV for the kinetic energy resolution. This represents a conservative estimate for the kinetic energy resolution achieved in the present experiment. The kinetic energy resolution is expected to be better for lower kinetic energy release. Here, this Gaussian instrumental profile with FWHM = 0.07 eV is used as the energy profile for single rotational excitations. The PGOPHER program[35] is employed to generate the best fitted Boltzmann rotational distributions [shown by blue dotted curves in Fig. 2(d)–(f)] for individual CO($X^1\Sigma^+$; v) vibrational bands observed in the TKER spectra. We note that the rotational fits are not unique. In a fast dissociative process, the rotational populations of CO($X^1\Sigma^+$; v) might not reach equilibrium, and thus the rotational distribution of CO photoproducts might not be able to be characterized by a rotational temperature. The simulated TKER spectra [red curves of Fig. 2(d)–(f)] represent the sum of the best rotational distribution fits of the vibrational bands associated with the same TKER spectrum. The simulation reveals that the CO($X^1\Sigma^+$; v = 0–9) photoproducts are rotationally hot with the FWHMs fall in the range of 0.2–0.3 eV. This observation of high rotational excitations is consistent with the picture that the VUV excited CO_2* molecules undergo some degree of bending vibrational motion along the exit pathways before departing to form CO($X^1\Sigma^+$; v) + O(^{1}S) photoproducts.

Fig. 3(a) compares the vibrational state distributions for CO($X^1\Sigma^+$; v = 0–9) photoproducts associated with the formation of O(^{1}S) in CO_2 photodissociation determined based on the rotational simulations of vibrational bands observed in the TKER spectra of Fig. 2(d)–(f). At the lowest photolysis energy, $h\nu$(VUV$_1$) = 12.125 eV, the CO($X^1\Sigma^+$; v = 0–9) vibrational state distribution is found to peak at the v = 1 state, whereas at slightly higher photon energies, $h\nu$(VUV$_1$) = 12.145 and 12.150 eV, the vibrational distributions are found to have the population peaked at the v = 0 state. The observation of the highest intensity for v = 1 at $h\nu$(VUV$_1$) = 12.125 eV can be considered as consistent with the formation of the CO_2*[4s(1_0^1)] predissociative state. Since the excited CO_2* molecule resulting from the Franck–Condon excitation in this VUV region has one vibrational quantum in the symmetric stretching mode, this vibrational excitation of CO_2 may affect the final vibrational distribution of CO($X^1\Sigma^+$; v) photoproducts, favoring the formation of the v = 1 state. Nevertheless, as the VUV excitation energy is increased, the CO_2 wavepacket may move to a different part of the excited PES giving rise to a monotonically decreasing population with increasing the CO($X^1\Sigma^+$; v) vibrational state.

Fig. 3(b) compares the plots of the measured anisotropy β parameters for process (3) *versus* the CO($X^1\Sigma^+$; v) vibrational levels determined at the three photon energies, $h\nu$(VUV$_1$) = 12.125, 12.145, and 12.150 eV. The anisotropy β parameter plots observed at these three VUV$_1$ energies are found to have similar trends, decreasing roughly monotonically from the values of 1.9–2.0 at v = 0 to 1.0–1.3 at v = 9. The observed β values are consistent with parallel transitions, indicating that the dissociation of excited CO_2* [4s(1_0^1)] states at $h\nu$(VUV$_1$) = 12.125–12.150 eV are prompt with dissociation lifetimes shorter than the rotational periods of excited CO_2* molecules. The differences in the

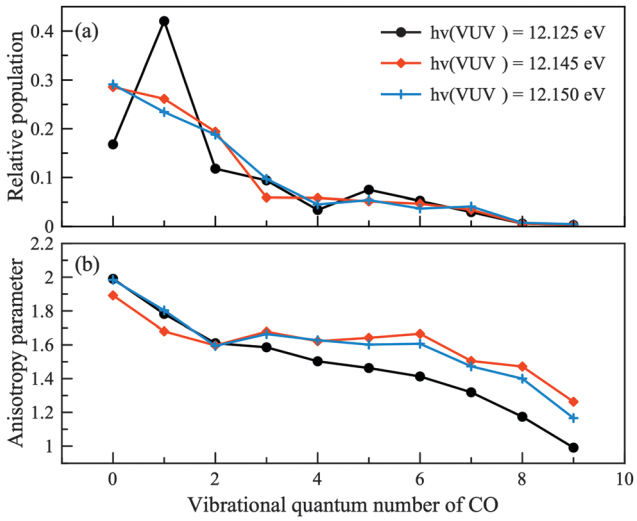

Fig. 3 (a) Comparison of the relative vibrational state populations of CO($X^1\Sigma^+$; v = 0–9) observed at CO_2 photodissociation energies of 97797.7 cm^{-1} (12.125 eV) in black, 97955.1 cm^{-1} (12.145 eV) in red, and 97998.1 cm^{-1} (12.150 eV) in blue. (b) Comparison of the vibrational state dependences of the β parameters for the formation of CO($X^1\Sigma^+$; v = 0–9) + O(^{1}S) photoproduct channels transformed from the measured O(^{1}S) VMI-PI images at CO_2 photodissociation energies of 97797.7 cm^{-1} (12.125 eV) in black, 97955.1 cm^{-1} (12.145 eV) in red, and 97998.1 cm^{-1} (12.150 eV) in blue.

vibrational populations of CO($X^1\Sigma^+$; v) photofragments formed at the three energies, $h\nu$(VUV$_1$) = 12.125, 12.145, and 12.150 eV, are likely the reflection of sampling different parts of the excited CO_2* PES. Nevertheless, the observation of similar β values at these VUV$_1$ energies is consistent with the conclusion that the same excited CO_2* [4s(1_0^1)] state is accessed at the photon energy range of $h\nu$(VUV$_1$) = 12.125–12.150 eV.

In order to further examine the dynamics for the formation of the CO($X^1\Sigma^+$) + O(^{1}S) channel, we have also recorded the time-sliced VMI-PI images of O(^{1}S) recorded at lower CO_2 VUV$_1$ excitation energies, $h\nu$(VUV$_1$) = 11.964, 11.989, and 11.994 eV, as depicted in Fig. 4(a)–(c), respectively. We have also marked these VUV$_1$ photon energies by downward pointing red arrows in Fig. 1(b). As pointed out above, the VUV$_1$ excitation of CO_2 at these energies is expected to populate the CO_2*(4s) Rydberg state at 11.967 eV and the unassigned absorption shoulder band at 11.985 eV.[33] Due to the lack of VUV$_1$ output at 11.974 eV, the excited CO_2*[3p$^1\Pi_u$(1_0^4)] state cannot be examined here. Similar to the observation at the excited CO_2*[4s(1_0^1)] state, the VMI-PI images of Fig. 4(a)–(c) also reveal that the formation of CO($X^1\Sigma^+$) + O(^{1}S) photoproducts is more rapid than the rotational period of the VUV$_1$ excited CO_2* molecules.

Fig. 4(d)–(f) show the TKER spectra (black curves) for CO($X^1\Sigma^+$) + O(^{1}S) transformed from the respective O(^{1}S) VMI-PI images of Fig. 4(a)–(c) along with the best simulations (red curves) of the TKER spectra. Similar to the TKER spectra of Fig. 2(d)–(f), the onsets of the TKER spectra of Fig. 4(d)–(f) are found to be in excellent accord with the known thermochemical threshold of process (3). By employing the simulation procedures described above, we have assigned the TKER spectra of Fig. 4(d)–(f) to the

 This journal is © the Owner Societies 2015

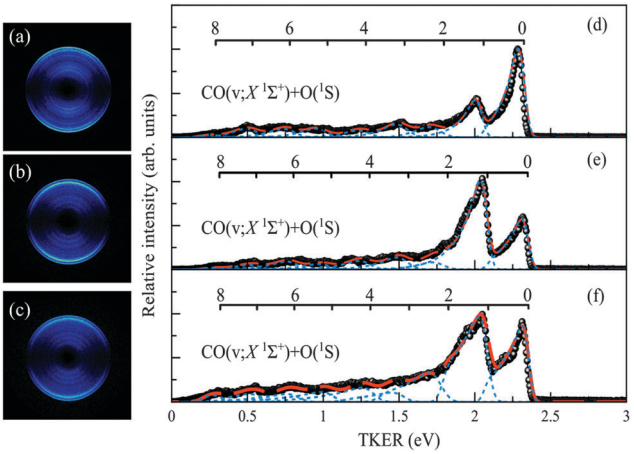

Fig. 4 Time-sliced VMI-PI images of $O(^1S)$ photofragments observed at CO_2 photoexcitation energies of (a) 96495.7 cm^{-1} (11.964 eV), (b) 96697.5 cm^{-1} (11.989 eV), and (c) 96738.8 cm^{-1} (11.994 eV) and their corresponding TKER spectra (black open-circle curves) shown in (d–f). Black drop lines on the TKER spectra designate the vibrational levels of the $CO(X^1\Sigma^+; v = 0–8)$ product. The vibrational state assignments are based on the simulated vibrational distributions (red curves), which represent the sum of individual simulated vibrational peaks (blue dashed lines).

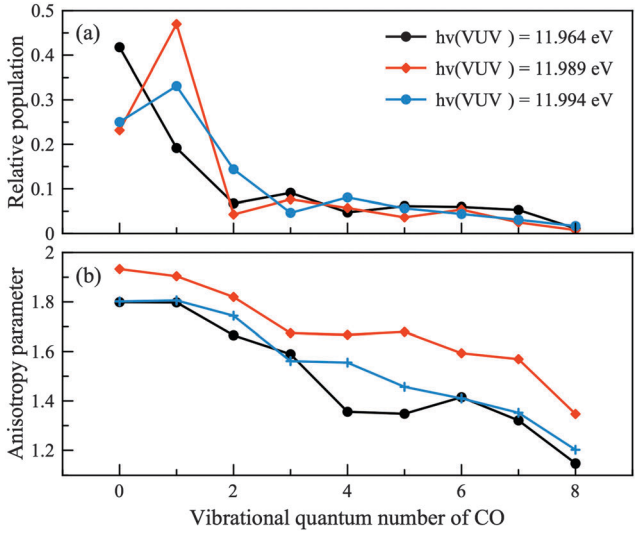

Fig. 5 (a) Comparison of the relative vibrational state populations of $CO(X^1\Sigma^+: v = 0–8)$ at CO_2 photodissociation energies of 96495.7 cm^{-1} (11.964 eV) in black, 96697.5 cm^{-1} (11.989 eV) in red, and 96738.8 cm^{-1} (11.994 eV) in blue. (b) Comparison of the β parameters for individual $CO(X^1\Sigma^+; v = 0–8)$ vibrational states transformed from the $O(^1S)$ VMI-PI images at CO_2 photodissociation energies of 96495.7 cm^{-1} (11.964 eV) in black, 96697.5 cm^{-1} (11.989 eV) in red, and 96738.8 cm^{-1} (11.994 eV) in blue.

population of $CO(X^1\Sigma^+; v = 0–9)$ vibrational states as marked on top of the spectra. At $h\nu(VUV_1)$ = 11.964 eV, the vibrational population of the $v = 0$ state is higher than those of all other $CO(X^1\Sigma^+; v)$ vibrational levels. At higher $h\nu(VUV_1)$ = 11.989 and 11.994 eV, the $v = 1$ state becomes the most populated.

The $CO(X^1\Sigma^+; v)$ vibrational state distributions (deduced based on the rotational simulation described above), which correlate with the formation of $O(^1S)$ at $h\nu(VUV_1)$ = 11.964, 11.989, and 11.994 eV, are compared in Fig. 5(a). This comparison shows that the measured anisotropy β parameters and their vibrational dependences also decrease from 1.8–1.9 to 1.1–1.4 as the vibrational state is increased from $v = 0$ to 8. This trend is similar to that observed for the $CO_2[4s(1_0{}^1)]$ predissociative state. Since the $CO_2(4s)$ Rydberg state and the unassigned absorption band are very close in energy, the observations of having similar $CO(X^1\Sigma^+; v)$ vibrational populations as well as β parameters may imply that the $O(^1S)$ VMI-PI images are resulted from sampling the same excited $CO_2^*(4s)$ electronic state or a similar local potential region. The comparison of the vibrational distributions of Fig. 3(a) and 5(a) shows that although both the vibrational distributions resulted from VUV_1 excitation at 12.125–12.150 and 11.964–11.985 eV favor the populations of the $v = 0$ and 1 states, the populations of higher vibrational states are found to become more favorable at higher VUV_1 energies.

C. The formation of the $O(^1D) + CO(X^1\Sigma^+)$ photoproduct channel

The $O(^1D)$ VMI-PI images are also recorded by employing two $O(^1D)$ autoionization detection schemes: $O^*[2s^22p^3(^2D^0{}_{3/2})3d(^1D^0{}_2)] \leftarrow O(^1D)$ at $h\nu(VUV_2)$ = 13.446 eV and $O^*[2s^22p^3(^2D^0{}_{3/2})4d(^1F^0{}_3)] \leftarrow O(^1D)$ at $h\nu(VUV_2)$ = 14.118 eV transitions. These two detection schemes generate similar O^+ ion intensities. As expected, that the $CO(X^1\Sigma^+; v)$ vibrational distributions obtained from $O(^1D)$ ion images are found to be independent of the detection schemes used. The time-sliced VMI-PI images of $O(^1D)$ photoproducts observed from CO_2 photodissociation at $h\nu(VUV_1)$ = 12.125, 12.145, and 12.150 eV are shown in Fig. 6(a)–(c), respectively. These $O(^1D)$ VMI-PI images reveal well-resolved anisotropic outer ring structures, which are indicative of relatively narrow rotational distributions for the low $CO(X^1\Sigma^+; v)$ vibrational states. The brighter inner circles imply that the rotational distributions are broader for higher $CO(X^1\Sigma^+; v)$ vibrational states.

Fig. 6(d)–(f) depict the $O(^1D)$ TKER spectra (black curves) transformed from the corresponding $O(^1D)$ VMI-PI images of Fig. 6(a)–(c). The observation that the onsets of these TKER spectra are consistent with the thermochemical threshold for process (2) indicates that these TKER spectra are associated with the formation of $O(^1D) + CO(X^1\Sigma^+; v)$. The TKER spectra reveal a series of vibrational bands with spacing of about 0.27 eV. We have assigned these bands to populations of the $CO(X^1\Sigma^+; v = 0–18)$ vibrational states as marked on top of the TKER spectra. We have also performed rotational fits to individual vibrational bands following the procedures described above. The simulated TKER spectra (red curves) represent the sum of all the simulated vibrational bands (blue curves) shown in Fig. 6(d)–(f). The FWHMs for the best fit to the rotational distributions for the observed $CO(X^1\Sigma^+; v)$ vibrational bands were found to be in the range of 0.3–0.35 eV. Since these FWHM values are wider than those found for $CO(X^1\Sigma^+; v)$ vibrational bands associated with the $O(^1S) + CO(X^1\Sigma^+; v)$ channel, we may conclude that $CO(X^1\Sigma^+; v)$ photofragments formed by process (2) are rotationally hotter than those produced by process (3). The observation of rotationally hot $CO(X^1\Sigma^+; v)$ photofragments

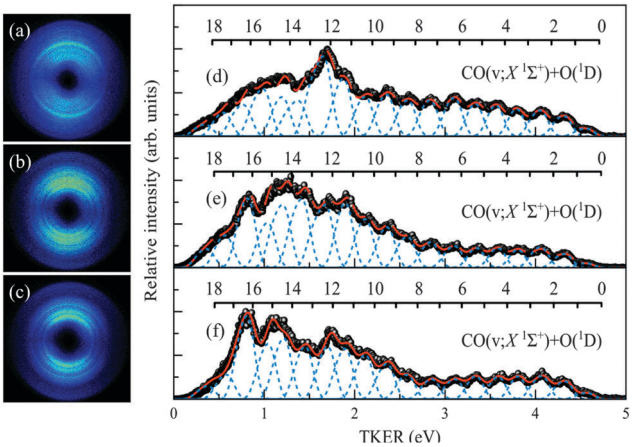

Fig. 6 Time-sliced VMI-PI images of O(^{1}D) photofragments recorded at CO_2 photoexcitation energies of (a) 97797.7 cm^{-1} (12.125 eV), (b) 97955.1 cm^{-1} (12.145 eV), and (c) 97998.1 cm^{-1} (12.150 eV) and their corresponding TKER spectra (black open-circle curves) shown in (d–f). Black drop lines on the TKER spectra designate the vibrational levels of the CO($X^1\Sigma^+$; v = 0–18) product. The vibrational state assignments are based on the simulated vibrational distributions (red curves), which represent the sum of individual simulated vibrational peaks (blue dashed lines).

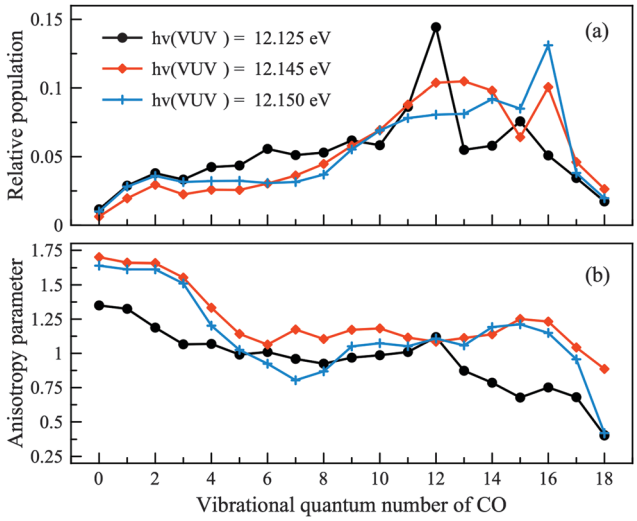

Fig. 7 (a) Comparison of the relative vibrational state populations CO($X^1\Sigma^+$; v = 0–18) observed at CO_2 photodissociation energies of 97797.7 cm^{-1} (12.125 eV) in black, 97955.1 cm^{-1} (12.145 eV) in red, and 97998.1 cm^{-1} (12.150 eV) in blue. (b) Comparison of the β parameters for individual CO($X^1\Sigma^+$; v = 0–19) vibrational state measured from the VMI-PI images of O(^{1}S) photofragments observed at CO_2 photodissociation energies 97797.7 cm^{-1} (12.125 eV) in black, 97955.1 cm^{-1} (12.145 eV) in red, and 97998.1 cm^{-1} (12.150 eV) in blue.

implies that VUV_1 excited CO_2* molecules may undergo finite bending vibrational motion, resulting in a OCO bond angle smaller than 180° during the dissociation to form O + CO photoproducts.

The extended vibrational excitation of v = 0–18 for the O(^{1}D) channel compared to that of v = 0–9 for the O(^{1}S) channel can be attributed to lower energetic threshold of process (2). The vibrational populations of CO($X^1\Sigma^+$; v) resolved in the TKER spectra for process (2) shown Fig. 6(d)–(f) are significantly more complex than those observed in the TKER spectra for process (3) of Fig. 2(d)–(f) and 4(d)–(f). Contrary to the CO($X^1\Sigma^+$; v) vibrational distributions observed for the O(^{1}S) channel, which peak at low v = 0 and 1 levels, the vibrational populations for CO($X^1\Sigma^+$; v) associated with the O(^{1}D) channel are found to peak at high (v = 11–16) vibrational levels. The more complex vibrational profiles for CO($X^1\Sigma^+$; v = 0–18) observed in Fig. 6(d)–(f) indicate that the dissociation dynamics for process (2) is distinctly different from that for process (3). The vibrational populations for CO($X^1\Sigma^+$; v = 0–18) obtained based on the rotational simulation of vibrational bands observed in the TKER spectra of Fig. 6(d)–(f) are compared in Fig. 7(a). This comparison shows that the vibrational populations for CO($X^1\Sigma^+$; v = 0–18) are highly sensitive to the VUV_1 excitation energy for CO_2, and thus should offer a sensitive probe of the CO_2 PESs.

Fig. 7(b) presents the anisotropy β parameters determined for different CO($X^1\Sigma^+$; v = 0–18) vibrational states based on the O(^{1}D) VMI-PI images recorded at $h\nu$(VUV_1) = 12.125, 12.145, and 12.150 eV. These vibrational dependences of β parameters for the O(^{1}D) channel are generally similar to those observed for the O(^{1}S) dissociation channel shown in Fig. 3(b) and 5(b), revealing a roughly decreasing trend with increasing the CO($X^1\Sigma^+$; v) vibrational state.

Fig. 8(a) and (b) depict the respective O(^{1}D) VMI-PI image and the corresponding TKER spectrum recorded in the photolysis

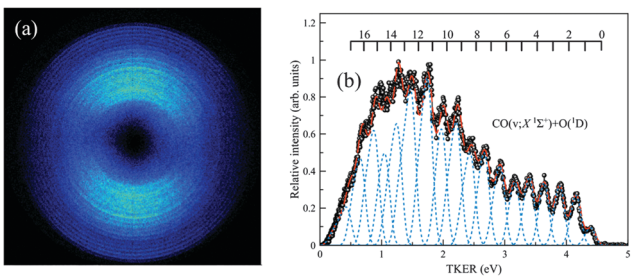

Fig. 8 (a) Time-sliced VMI-PI image of O(^{1}D) photofragments recorded at CO_2 photoexcitation energy of 11.989 eV. (b) The TKER spectrum (black, open-circle curves) for the formation of O(^{1}D) + CO($X^1\Sigma^+$; v = 0–17) deduced from the O(^{1}D) images of (a). The CO($X^1\Sigma^+$; v = 0–17) vibrational state assignments are marked on top of the TKER spectra. The simulated TKER spectrum (red curves) represents the sum of all rotational-simulated vibrational peaks (blue dotted curves) of the same TKER spectrum.

of CO_2 at $h\nu$(VUV_1) = 11.989 eV. Similar to the observation of the TKER spectra of Fig. 6(d)–(f), we find that the onset for the TKER spectrum of Fig. 8(b) is in good agreement with the thermochemical threshold of process (2). The simulation of the TKER spectrum allows us to assign the formation of CO($X^1\Sigma^+$; v = 0–17) vibrational states as marked in Fig. 8(b), and to determine the relative vibrational distribution of CO($X^1\Sigma^+$; v = 0–17) as plotted in Fig. 9(a). This CO($X^1\Sigma^+$; v) photoproduct vibrational population is similar to that observed in Fig. 7(a), which are found to have the maximum at CO($X^1\Sigma^+$; v = 11–13). Furthermore, the measured vibrational dependences of the β parameters plotted in Fig. 7(b) and 9(b) are also alike, possibly indicates that the dissociation mechanisms are for the formation of the O(^{1}D) + CO($X^1\Sigma^+$) are similar.

 This journal is © the Owner Societies 2015

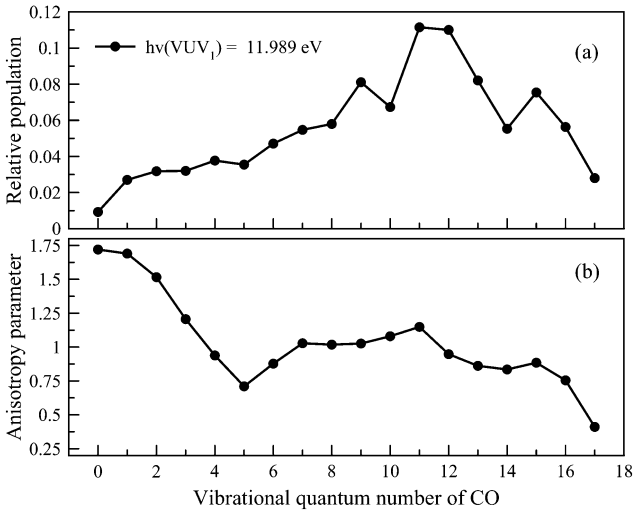

Fig. 9 (a) Relative CO($X^1\Sigma^+$; v = 0–17) vibrational populations derived from the rotational-simulated experimental TKER spectrum. (b) The anisotropy β parameters for individual CO($X^1\Sigma^+$; v = 0–17) vibrational bands obtained from the analysis of O(^{1}D) VMI-PI image of (a).

D. Theoretical results and interpretation

We have examined[36] the one-dimensional cuts of the MRCI/aug-cc-pV5Z PESs of the singlet electronic states of CO_2 by lengthening one CO distance [r_1(CO)] distance for several OCO bond angles with the other r_2(CO) distance held constant in the range of 2.0–2.9 Bohr (1 Bohr = 0.53 Å). These calculations show that the major electronic states involved in the present photodissociation experiment, which is concerned with the formation of the spin allowed O(^{1}D) + CO($X^1\Sigma^+$; v) and O(^{1}S) + CO($X^1\Sigma^+$; v) channels, are the 3^1A′ and 4^1A′ PESs.

Fig. 10(a)–(j) displays the MRCI/aug-cc-pV5Z two-dimensional evolutions of the 3^1A′ and 4^1A′ PESs of CO_2 calculated as a function of the r_1(CO) distance and the OCO bond angle, with the other r_2(CO) distance fixed at 2.0, 2.1, 2.2, 2.3 and 2.4 Bohr. The OCO bond angle range covered in these PESs is from 160° to 180°. The 3^1A′ PESs are shown in Fig. 10(a), (c), (e), (g) and (i) while the 4^1A′ PESs are presented in Fig. 10(b), (d), (f), (h) and (j). The 3^1A′ and 4^1A′ PESs asymptotically correlate to the O(^{1}D) + CO($X^1\Sigma^+$; v) and O(^{1}S) + CO($X^1\Sigma^+$; v) channels, respectively. The energies of these PESs are measured with respect to the energy minimum of the potential energy curve for the CO_2($X^1\Sigma_g^+$) ground state. Here, the lower singlet A′ and the singlet A″ states are not shown in Fig. 10(a)–(j) because they are not of directly relevance to the present photodissociation study, which are concerned with the formation of the O(^{1}D) + CO($X^1\Sigma^+$; v) and O(^{1}S) + CO($X^1\Sigma^+$; v) channels. The region on the 4^1A′ excited PES that can be accessed by the Franck–Condon (FC) excitation from the ground state of CO_2 is marked with a yellow star in the PESs of Fig. 10(d) and (f). This position of the excited 4^1A′ PES can be considered as the starting point of the CO_2 dissociation, which is expected to give the O(^{3}P), O(^{1}S) and O(^{1}D) atomic photofragments *via* processes (1)–(4) at the $h\nu$(VUV$_1$) of 11.95–12.22 eV. Since the formation of the O(^{3}P) channels [processes (1) and (4)] has been reported previously,[12] the present study is focused on the production of O(^{1}D) and O(^{1}S), *i.e.*, processes (2) and (3). The formation of the O(^{3}P) + CO($X^1\Sigma^+$) channel necessarily involves the triplet manifolds of CO_2 PESs. As shown below, the present MRCI calculations show that the formation of O(^{3}P) + CO($a^3\Pi$) is correlated to the 3^1A″ PES of CO_2.

Fig. 10(a)–(j) show that the shapes of the 3^1A′ and 4^1A′ PESs are not regular. The 4^1A′ PES is generally downhill with ripples of minor potential energy barriers as r_1(CO) is increased. The ripple of minor potential energy barriers are resulted from avoided crossings between the close lying A′ states. Considering that the slope of the 4^1A′ PES in the vicinity of the FC accessed region is large, rapid CO_2 predissociation is to be expected. Without detailed dissociation dynamics calculations, the calculated 4^1A′ PES suggests that the dissociation pathway may follow the downhill direction as marked by the yellow arrows in PESs of Fig. 10(d), (f), (h) and (j), leading to the formation of O(^{1}S) + CO($X^1\Sigma^+$; v).

A key feature of the 3^1A′ and the 4^1A′ PESs shown in Fig. 10(a)–(e) is the seam of conical intersections of the two PESs located at r(CO) ∼ 3.5 Bohr. This gives rise to a ridge of potential energy barrier at a range OCO bending angles on the 3^1A′ PES and the corresponding trench on the 4^1A′ PES at r_1(CO) ∼ 3.5 Bohr. A ridge of minor potential energy barriers is also observed in the 4^1A′ PES at slightly larger r_1(CO) distance. This small potential energy barrier of the 4^1A′ state almost vanishes for r_1(CO) ∼ 3.5 Bohr, r(CO)$_2$ ∼ 2.1–2.2 Bohr, and bending angles of ∼165–170°. Both the conical intersection between the 3^1A′ and the 4^1A′ states and the minor potential barrier on the 4^1A′ state are found to be at higher energies if the fixed CO distance r_2(CO) is <2.1 or >2.3 Bohr.

To further illustrate the PESs that are important for understanding the CO_2 photodissociation mechanisms, we show in Fig. 11 a one-dimensional evolution of the lowest singlet electronic states of CO_2, including the 1^1A′, 2^1A′, 3^1A′, and 4^1A′ as well as the 1^1A″, 2^1A″ and 3^1A″ PESs along the r_1(CO) distance at a close to linear OCO configuration, where the r_2(CO) distance is fixed to its equilibrium value of 2.2 Bohr in the CO_2($X^1\Sigma_g^+$) ground state. This figure shows that with the exception of the 1^1A′ PES, all other states have irregular shapes, resulting from avoided crossings. The 1^1A′, 2^1A′, and 3^1A′ states, the 1^1A″, and 2^1A″ states also correlate with the O(^{1}D) + CO($X^1\Sigma^+$) channel. Fig. 11 also shows that the formation of CO($a^3\Pi$) + O(^{3}P) [process (4)] is predicted to correlate with the 3^1A″ state. The location of the conical intersection between the 3^1A′ and the 4^1A′ states is shown by the dotted circle; and the minor potential energy barrier of the 4^1A′ state is marked by the red downward pointing arrow in Fig. 11. The dotted vertical line shows the center of the FC vertical transition region from the CO($X^1\Sigma^+$) ground state. Both features evolve along the r_1(CO) and r_2(CO) distances and the OCO bending angle as shown in the 3^1A′ and the 4^1A′ PESs of Fig. 10(a)–(e).

The existence of the conical intersection seam at r_1(CO) ∼ 3.5 Bohr is expected to facilitate the transition of the excited CO_2* complex from the 4^1A′ to the 3^1A′ PES. As a result, two dissociation pathways may be expected for CO_2* dissociation beginning from the FC accessed region of the 4^1A′ PES. As pointed

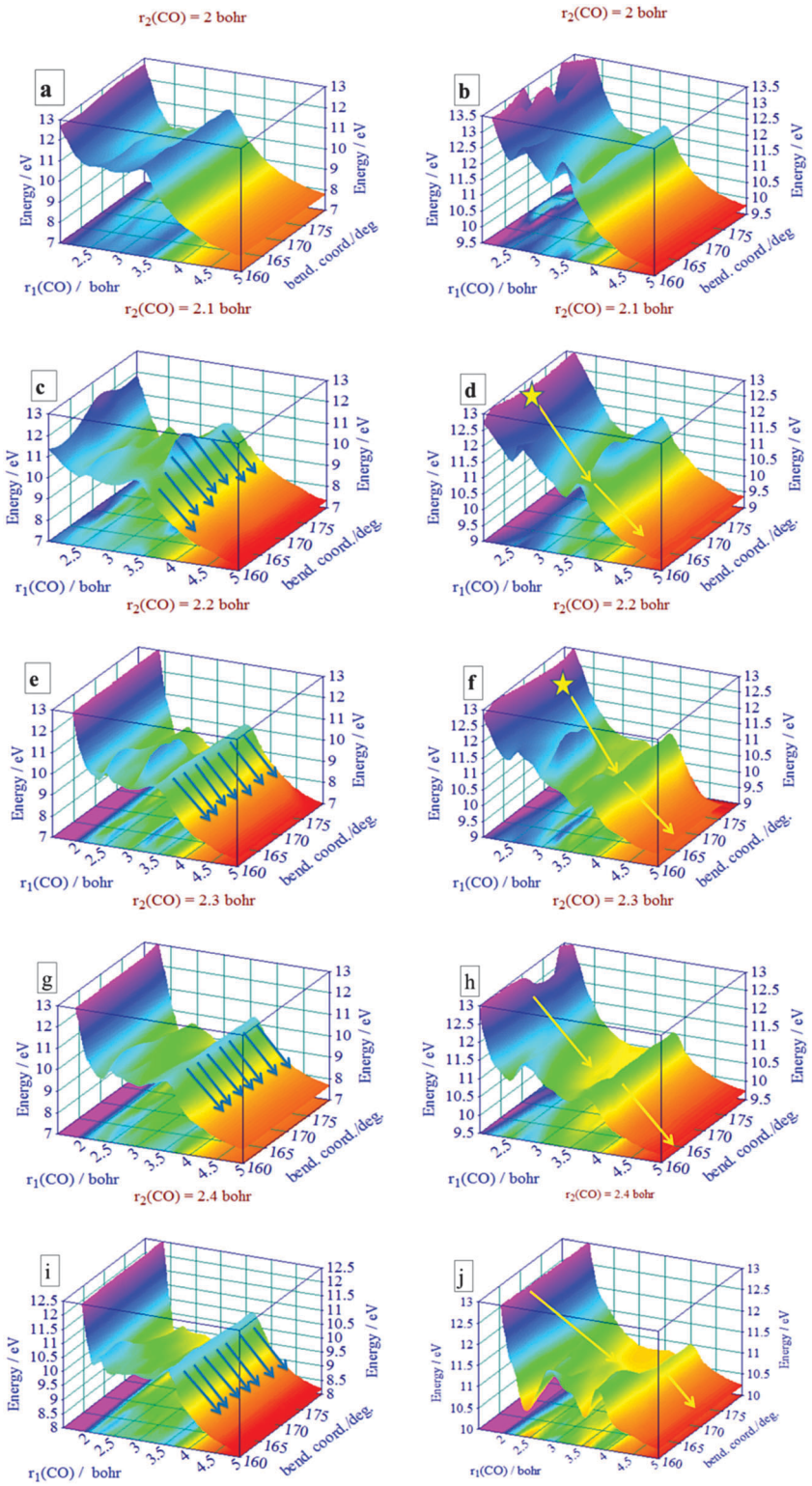

Fig. 10 Bi-dimensional evolutions of the MRCI/aug-cc-pV5Z PESs of the $3^1A'$ and $4^1A'$ states of CO_2 along the r_1(CO) and the OCO bending angles, where the distance is fixed in the range of 2.0–2.4 Bohr. The $3^1A'$ PESs calculated at r_2(CO) = 2.0, 2.1, 2.2, 2.3, and 2.4 Bohr are shown in (a), (c), (e), (g), and (i), and the $4^1A'$ PESs calculated at r_2(CO) = 2.0, 2.1, 2.2, 2.3, and 2.4 Bohr are shown in (b), (d), (f), (h), and (j). The energies are given with respect to the energy of CO_2 ground state. The yellow star shows the Franck Condon accessed region by VUV_1 photoexcitation from the ground state of CO_2. The yellow arrows illustrate the possible dissociation pathway leading to the formation of $O(^1S)$ + $CO(X^1\Sigma^+; v)$.

out above, one is to follow the reaction path along the $4^1A'$ PES as indicated by the yellow arrows in Fig. 10(d), (f), (h) and (j), which should lead to a rapid, direct fragmentation mechanism, giving rise to the formation of $CO(X^1\Sigma^+)$ + $O(^1S)$ photoproducts.

 This journal is © the Owner Societies 2015

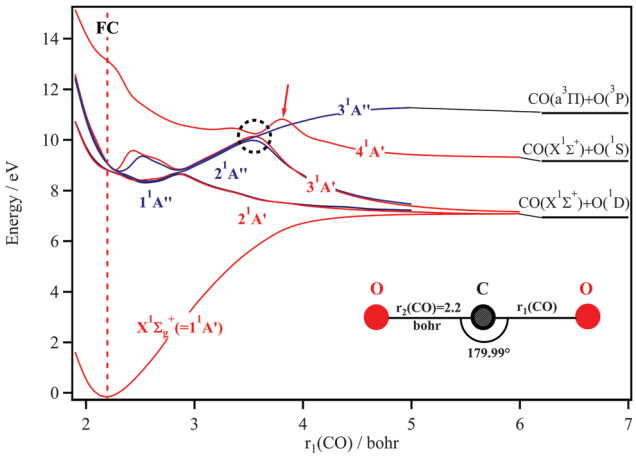

Fig. 11 One-dimensional evolution of the PESs of the lowest singlet electronic states of CO_2 along the r(CO) distance for close to linear configuration and where the other CO distance is fixed to its equilibrium value of 2.2 Bohr in $CO_2(X^1\Sigma_g^+)$. The red dash line FC marks the center of the Franck–Condon transition region. The black dash circle highlights the conical intersection between the $3^1A'$ and the $4^1A'$ states. The red arrow points out the small potential barrier of the $4^1A'$ state along the $CO(X^1\Sigma^+)$ + $O(^1S)$ channel. Both features evolve along the CO distances and the bending angle. This is given for the $3^1A'$ and the $4^1A'$ states in Fig. 10.

The other mechanism may involve non-adiabatic transitions of excited CO_2* from the $4^1A'$ to the $3^1A'$ PES *via* the seam of conical intersections. The formation of $CO(X^1\Sigma^+)$ + $O(^1D)$ photoproducts should follow by the downhill pathways as marked by the blue arrows on the $3^1A'$ PESs of Fig. 10(c), (e), (g), and (i). The higher rotational and vibrational excitations observed for the $CO(X^1\Sigma^+)$ photoproducts associated with the $O(^1D)$ channel as compared to that for the $O(^1S)$ channel are consistent with the theoretical prediction that excited CO_2* complexes with a wide range of OCO bending angle (165–180°) are formed by the conical intersection transitions from the $4^1A'$ to the $3^1A'$ PES. The subsequent dissociation pathways of these CO_2* complexes along the $3^1A'$ PES (marked by blue arrows) is expected to result in the formation of the $O(^1D)$ channel with a wide range of rotational and vibrational excitations for the counter $CO(X^1\Sigma^+)$ photoproducts. The photodissociation mechanisms presented here for the formation of the $O(^1S)$ + $CO(X^1\Sigma^+)$ and $O(^1D)$ + $CO(X^1\Sigma^+; v)$ channels imply that the dissociation lifetime for the $O(^1S)$ channel is shorter than that for the $O(^1D)$ channel. This implication is consistent with the experimental anisotropy β parameters obtained for processes (2) and (3).

V. Conclusion

By combining two independently tunable VUV laser sources with a time-sliced velocity-map imaging detector, we have detected the spin-allowed $CO(X^1\Sigma^+)$ + $O(^1D)$ and $CO(X^1\Sigma^+)$ + $O(^1S)$ photoproduct channels from CO_2 photodissociation at $h\nu$(VUV) = 11.94–12.20 eV. For the $CO(X^1\Sigma^+)$ + $O(^1S)$ dissociation channel, most of $CO(X^1\Sigma^+; v)$ photofragments are found to populate low (v = 0–2) vibrational states. For the $CO(X^1\Sigma^+; v)$ + $O(^1D)$ channel, the majority of $CO(X^1\Sigma^+; v)$ photoproducts are shown to populate high (v = 11–16) vibrational states. The β parameters measured from the $O(^1S)$ and $O(^1D)$ VMI-PI images indicate prompt CO_2 photodissociation with the dissociation lifetime shorter than the rotational period of the VUV excited CO_2* complex. The comparison of the β parameters observed for the $O(^1S)$ and $O(^1D)$ photofragments reveals that the dissociation lifetime for the $CO(X^1\Sigma^+)$ + $O(^1S)$ channel is generally shorter than that for the $CO(X^1\Sigma^+)$ + $O(^1D)$ and channel. The singlet $3^1A'$ and $4^1A'$ PESs, which are relevant to the present photodissociation study, have been calculated at the MRCI level of theory. The PESs thus obtained support the experimental observation that the CO_2 dissociation to produce the $O(^1S)$ and $O(^1D)$ channels are prompt. The calculated PESs also suggest that the formation of the $O(^1S)$ channel occurs predominantly on the essentially repulsive $4^1A'$ PES, whereas the $O(^1D)$ channel may be produced by non-adiabatic transition from the $4^1A'$ to the $3^1A'$ PES *via* conical intersections followed by the rapid formation of $CO(X^1\Sigma^+)$ + $O(^1D)$ along the $3^1A'$ PES.

Acknowledgements

W. M. Jackson acknowledges the support of the National Science Foundation (NSF) under Grant No. CHE-1301501. C. Y. Ng acknowledges the support by the Chemical Sciences, Geosciences and Biosciences Division, Office of Basic Energy Sciences, Office of Science, (U.S.) Department of Energy (DOE) under Contract No. DE-FG02-02ER15306. We also thank Glenn Stark at Wellesley College for providing the digitized CO_2 high-resolution photoabsorption spectrum. M.H. A.B.H. and T.A. are thankful for a Marie Curie International Research Staff Exchange Scheme Fellowship within the 7th European Community Framework Program under Grant No. PIRSES-GA-2012-31754 and the COST Action CM1405 MOLIM. This study was undertaken while M.H. was a Visiting Professor at King Saud University. The support of the Visiting Professor Program at King Saud University is hereby gratefully acknowledged.

References

1 J. Emmert, M. Stevens, P. Bernath, D. Drob and C. Boone, *Nat. Geosci.*, 2012, **5**, 868–871.
2 M. B. McElroy, N. Dak Sze and Y. Ling Yung, *J. Atmos. Sci.*, 1973, **30**, 1437–1447.
3 A. Anbar, M. Allen and H. Nair, *J. Geophys. Res.*, 1993, **98**, 10925–10931.
4 M. Hässig, K. Altwegg, H. Balsiger, A. Bar-Nun, J. Berthelier, A. Bieler, P. Bochsler, C. Briois, U. Calmonte and M. Combi, *Science*, 2015, **347**(6220), aaa0276.
5 W. Chan, G. Cooper and C. Brion, *Chem. Phys.*, 1993, **178**, 401–413.
6 G. M. Lawrence, *J. Chem. Phys.*, 1972, **56**, 3435–3442.
7 G. M. Lawrence, *J. Chem. Phys.*, 1972, **57**, 5616–5617.
8 T. Slanger, R. Sharpless and G. Black, *J. Chem. Phys.*, 1977, **67**, 5317–5323.

9 K. S. Kalogerakis, C. Romanescu, M. Ahmed, K. R. Wilson and T. G. Slanger, *Icarus*, 2012, **220**, 205–210.
10 Y. Pan, H. Gao, L. Yang, J. Zhou, C. Y. Ng and W. M. Jackson, *J. Chem. Phys.*, 2011, **135**, 071101.
11 Y. Song, H. Gao, Y. C. Chang, Z. Lu, C. Y. Ng and W. M. Jackson, *Phys. Chem. Chem. Phys.*, 2014, **16**, 563–569.
12 Z. Lu, Y. C. Chang, H. Gao, Y. Benitez, Y. Song, C. Y. Ng and W. M. Jackson, *J. Chem. Phys.*, 2014, **140**, 231101.
13 Z. Lu, Y. C. Chang, Q.-Z. Yin, C. Y. Ng and W. M. Jackson, *Science*, 2014, **346**(6205), 61–64.
14 D.-Y. Hwang and A. M. Mebel, *Chem. Phys.*, 2000, **256**, 169–176.
15 J. A. Schmidt, M. S. Johnson and R. Schinke, *Proc. Natl. Acad. Sci. U. S. A.*, 2013, **110**, 17691–17696.
16 S. Y. Grebenshchikov, *J. Chem. Phys.*, 2013, **138**, 224106.
17 S. Y. Grebenshchikov, *J. Chem. Phys.*, 2012, **137**, 021101.
18 J. Zhou, K.-C. Lau, E. Hassanein, H. Xu, S.-X. Tian, B. Jones and C. Y. Ng, *J. Chem. Phys.*, 2006, **124**, 034309.
19 C. Y. Ng, *Annu. Rev. Phys. Chem.*, 2014, **65**, 197–224.
20 H. Gao, Y. Song, W. M. Jackson and C. Y. Ng, *J. Chem. Phys.*, 2013, **138**, 191102.
21 H. J. Werner and P. J. Knowles, *MOLPRO (version 2012.1) is a package of ab initio programs*, further details at www.molpro.net.
22 T. H. Dunning Jr, *J. Chem. Phys.*, 1989, **90**, 1007–1023.
23 R. A. Kendall, T. H. Dunning Jr and R. J. Harrison, *J. Chem. Phys.*, 1992, **96**, 6796–6806.
24 D. E. Woon and T. H. Dunning Jr, *J. Chem. Phys.*, 1993, **98**, 1358–1371.
25 D. E. Woon and T. H. Dunning Jr, *J. Chem. Phys.*, 1995, **103**, 4572–4585.
26 T. H. Dunning Jr, *J. Chem. Phys.*, 1989, **90**, 1007–1023.
27 P. J. Knowles and H.-J. Werner, *Chem. Phys. Lett.*, 1985, **115**, 259–267.
28 H. J. Werner and P. J. Knowles, *J. Chem. Phys.*, 1985, **82**, 5053–5063.
29 P. J. Knowles and H.-J. Werner, *Chem. Phys. Lett.*, 1988, **145**, 514–522.
30 H. J. Werner and P. J. Knowles, *J. Chem. Phys.*, 1988, **89**(9), 5803–5814.
31 L. Archer, G. Stark, P. Smith, J. Lyons, N. de Oliveira, L. Nahon, D. Joyeux and D. Blackie, *J. Quant. Spectrosc. Radiat. Transfer*, 2013, **117**, 88–92.
32 V. H. Dibeler and J. A. Walker, *Int. J. Mass Spectrom. Ion Phys.*, 1973, **11**, 49–56.
33 C. Cossart-Magos, M. Jungen and F. Launay, *Mol. Phys.*, 1987, **61**, 1077–1117.
34 Z. Chen, F. Liu, B. Jiang, X. Yang and D. H. Parker, *J. Phys. Chem. Lett.*, 2010, **1**, 1861–1865.
35 C. M. Western, *PGOPHER, a Program for Simulating Rotational Structure (version 8.0 2014)*, University of Bristol, http://pgopher.chm.bris.ac.uk.
36 See ESI† for the full set of the potential energy curves evolution of the lowest electronic states of CO_2.

 This journal is © the Owner Societies 2015